DRT analysis and transmission line modeling of ceria based electrodes for solid oxide cells

F. Kullmann [a], M. Mueller [a], A. Lindner [a], S. Dierickx [b], E. Mueller [c], A. Weber [a,*]

[a] Institute for Applied Materials (IAM-ET), Karlsruhe Institute of Technology (KIT), D-76131, Karlsruhe, Germany
[b] Robert Bosch GmbH, D-70049, Stuttgart, Germany
[c] Laboratory for Electron Microscopy (LEM), Karlsruhe Institute of Technology (KIT), D-76131, Karlsruhe, Germany

HIGHLIGHTS

- Identification of loss processes by distribution of relaxation times.
- Physicochemically meaningful impedance model for a single phase GDC fuel electrode.
- Impedance model enables access to charge transfer resistance at the GDC-surface.

ARTICLE INFO

Keywords:
Distribution of relaxation times
Electrochemical impedance spectroscopy
4-Point dc measurement
Focused ion beam-tomography
SOFC
Transmission line model

ABSTRACT

For the analysis of performance limiting processes in various electrochemical systems like lithium ion batteries, polymer electrolyte membrane fuel cells or solid oxide cells, impedance spectroscopy is a powerful tool. The distribution of relaxation times (DRT) enables the deconvolution of the polarization processes in the spectrum. The simple approach, to correlate each peak in the DRT with a single polarization process fails for multiphase electrodes as the complex coupling of electronic, ionic and transport of different species by spatially distributed charge transfer reactions leads to a number of correlated peaks in the DRT.

In this contribution such coupling of transport and reaction is analyzed for ceria based fuel electrodes applied in solid oxide cells. A physicochemically meaningful two-channel transmission line model is developed. Due to the ambiguity of impedance spectra and DRT, the straightforward approach of fitting this model to measured spectra does not allow an unambiguous model parameterization. Additional methods as conductivity measurements and focused ion beam-tomography are indispensable to obtain physicochemically meaningful parameters to be applied in the fitting procedure. With this parameterization approach DRT based modeling becomes feasible and ionic/electronic transport resistances and area specific charge transfer resistance of the ceria surface can be quantified.

1. Introduction

One key part for manufacturing high performance electrochemical systems is the understanding of the electrochemical processes in the cell and the impact of different parameters as material and microstructural properties, operating conditions or aging phenomena. Since decades, electrochemical impedance spectroscopy (EIS) is the method of choice to investigate the performance limiting processes in different electrochemical applications like lithium-ion batteries (LiB), polymer electrolyte membrane fuel cells (PEMFC) or solid oxide cells (SOC). For the separation and quantification of the individual loss processes in the spectrum, the distribution of relaxation times (DRT) analysis [1] and a subsequent complex nonlinear least squares (CNLS) fitting [2] based on an equivalent circuit model (ECM) are well-established [3–5].

The most simple approach of DRT-usage is based on the assumption that each peak in the DRT can be attributed to a single polarization process and vice versa each polarization process can be solely attributed to a single peak. This approach fails for any kind of well-designed multiphase electrode with spatially distributed reactions. The complex coupling of electronic, ionic and gas phase transport by the spatially distributed charge transfer reactions within the active electrode layer as well as the coupling of diffusive gas transport and storage in porous gas

* Corresponding author.
E-mail address: andre.weber@kit.edu (A. Weber).

diffusion layers or cell supports lead to multiple peaks in the DRT. The related equivalent circuits are of transmission line type as the Gerischer- or Warburg-impedance, their DRTs comprise a main peak and a number of smaller peaks at higher relaxation frequencies [6,7], which impede a straightforward DRT analysis.

Different studies showed the potential of a transmission line model (TLM) [8,9] in order to quantify the electrochemistry of porous electrodes in LiB [4,10], PEMFC [5,11,12] or SOC. In the latter, different electrode materials were investigated such as LSCF [13,14], Ni/YSZ [3, 15–17], Ni/ScYZ [18], LSM/YSZ [17,19,20], and Ni/GDC [21–24]. All the models include resistance contributions of transport phenomena as ionic, electronic and/or gas phase transport and their coupling by a charge transfer reaction or storage term. In most studies a one-channel transmission line model is used since the effective electronic conductivity is much higher than the ionic counterpart and gas diffusion within the penetration depth of a few µm is negligible.

State of the art fuel electrodes in solid oxide cells usually consist of porous ceramic electrolyte/metallic nickel compounds (cermets) with three interpenetrating matrices for ionic (yttria stabilized zirconia), electronic (nickel) and gas transport (pores). The charge transfer reaction is restricted to the three phase boundaries. In case of a nickel/ceria-cermet electrode, next to the three phase boundaries the double phase boundaries (ceria/gas) can contribute to the charge transfer reaction as ceria is a mixed conductor under reducing conditions [25–27]. In any case a well-designed Ni-matrix provides a very low electronic resistance that can be neglected in TLM-modeling.

In this study porous single-phase gadolinia doped ceria (GDC) fuel electrodes contacted by a porous single-phase nickel current collector layer [28] are investigated. The application of GDC as a single-phase fuel electrode is possible [28–31] since it shows a mixed ionic-electronic conductivity (MIEC) in reducing atmosphere [25–27]. This enables not only the electronic path in the GDC, but also the charge transfer reaction at the GDC/pore-interface (double phase boundary, DPB). Since GDC has a comparably low electronic conductivity, that is depending on temperature and oxygen partial pressure (fuel gas composition), the electronic transport resistance can no longer be neglected and the application of a two-channel transmission line model becomes necessary. The sole fitting of the TLM to measured spectra provides ambiguous parameters. Considering the TLM-equation, different model parameter sets result in identical spectra. Thus a number of model parameters must be determined separately in advance. In this work DRT-analysis and CNLS-fitting are supported by different methods as 4-point dc measurement and focused ion beam (FIB) tomography to predetermine microstructural and electrical parameters, mandatory for a physicochemically meaningful model parameterization.

2. Experimental

2.1. Investigated samples

For impedance measurements symmetrical cells based on an approximately 200 µm thick 8YSZ (8 mol.% yttria stabilized zirconia, 8YSZ) electrolyte-support (*ITOCHU Ceratech Corporation, Japan*) were manufactured. On both sides of the electrolyte a 20 mol.% gadolinia-doped ceria ($Ce_{0.8}Gd_{0.2}O_{2-\delta}$) layer with an area of 1 cm^2 was screen-printed (*EKRA-screen-printer, ASYS, Germany*) and sintered at 1100 °C for 3 h (*Nabertherm, Germany*). The paste was supplied by research center Jülich in Germany. The layer thickness is approximately 5 µm. In the next step a NiO-contact layer (*Kceracell, South Korea*) was screen-printed. The contact layer is applied to guarantee a sufficient in-plane conductivity and a homogeneous contact between GDC-layer and nickel contact mesh [28]. After a reduction at 800 °C, where the NiO is reduced to Ni, the sample was operated at 700 °C in 50 % H_2 and 50 % H_2O till stabilization of the impedance. It should be considered that most likely during the reduction process and/or the subsequent operation nickel from the contact layer diffuses into the GDC-layer and activates the GDC surface.

The sample for the conductivity measurements consists of a MgO support substrate (*Robert Bosch GmbH, Germany*) with a screen-printed porous GDC layer ($Ce_{0.8}Gd_{0.2}O_{2-\delta}$) sintered at 1300 °C for 3 h. The layer has a thickness of ~7 µm and a measured area of 0.85 cm^2. After the sintering process of the GDC layer, Pt-electrodes were applied and sintered at 1050 °C for 1 h.

2.2. Electrical and electrochemical characterization

The test setup used for the SOCs is described in Ref. [32]. In the symmetrical setup nickel meshes are applied on both sides of the symmetrical cell for contacting. The cell is located in one gas chamber with a total flow of 500 sccm. The impedance measurements are conducted without bias current by a Solartron 1260 in galvanostatic mode and the amplitude of the sinusoidal stimulus is chosen in order to receive a voltage response of the electrode of $\leq$ 12 mV [32]. The frequency ranges from 30 mHz to 1 MHz. The quality of the impedance spectra was checked by the Kramers Kronig validity test [33] revealing errors $<$ 1 %. Operating parameters as temperature (600 ... 700 °C) and fuel gas composition were gradually changed for sensitivity analysis and model parameterization. The stability was regularly checked by reference impedance measurements revealing a degradation in polarization resistance $<$ 5 %.

The conductivity sample is investigated in a 4-point dc measurement setup as pictured in Fig. 7 (b). The current input is realized by a 0.2 mm Pt-wire which is wrapped around the outer sintered Pt-electrodes. The voltage is measured between two Pt-electrodes. The distance between these two electrodes is 12 mm. The maximum voltage between the outer electrodes is set to 0.9 V to avoid any damage of the GDC layer. For the dc current stimulus, a Keithley 220 current source was used. The voltage measurement was performed by a Keysight 34970A digital multimeter.

2.3. FIB-SEM tomography

FIB/SEM tomography is used to analyze and reconstruct the microstructure of the porous GDC layers and determine the parameters tortuosity τ_{GDC} and volume fraction ε_{GDC}.

For high resolution FIB/SEM tomography the samples were carefully cracked into smaller ($<5 \times 5$ mm) pieces and vacuum infiltrated with a two-component epoxy resin (*Struers, Germany*) inside a vacuum infiltration chamber (*CitoVac, Struers, Germany*). Infiltration of the pore space both increases contrast during imaging and milling quality during the Slice&View process. Thin layers of platinum and amorphous carbon are deposited on the top of the sample to increase milling quality and to prevent any charging effects induced by the electron or ion beam. Any further processing and measurements of the fuel electrode are performed inside a Zeiss 1540 XB (*Zeiss Microscopy, Germany*) which is equipped with a Ga^+ ion source. Firstly, the sample is moved into the coincident point between electron and ion beam. Here, a rough region of interest is identified and an initial cross section is milled using a high beam current of 10 nA. After choosing the area of interest for the tomography, the sample is precisely moved into the eucentric point to perform the Slice&View process. Slices with a width of 10 nm are milled perpendicular to the sample surface with a fine beam of 500 pA. The imaging of the slices is performed with an accelerating voltage of 1.3 kV in a dual detector setup to obtain two datasets simultaneously. Acquisition is set to roughly 1 min per image using a pixel size of 10 nm. Overall, 460 images of the fuel electrode (Fig. 1 a, inlens detector) are obtained for each detector with a depth spacing of 20 nm.

For the reconstruction of the conductivity sample an identically manufactured GDC layer applied on an 8YSZ-substrate was prepared. The Ga^+-FIB milling and the imaging were performed in a Thermo Fisher DualBeam Helios G4 FX microscope. For rough milling, a beam current of 9–20 nA was used and 1.2 nA for cutting during the slice imaging. In total 700 images were taken at the accelerating voltage of 3.0 kV by an

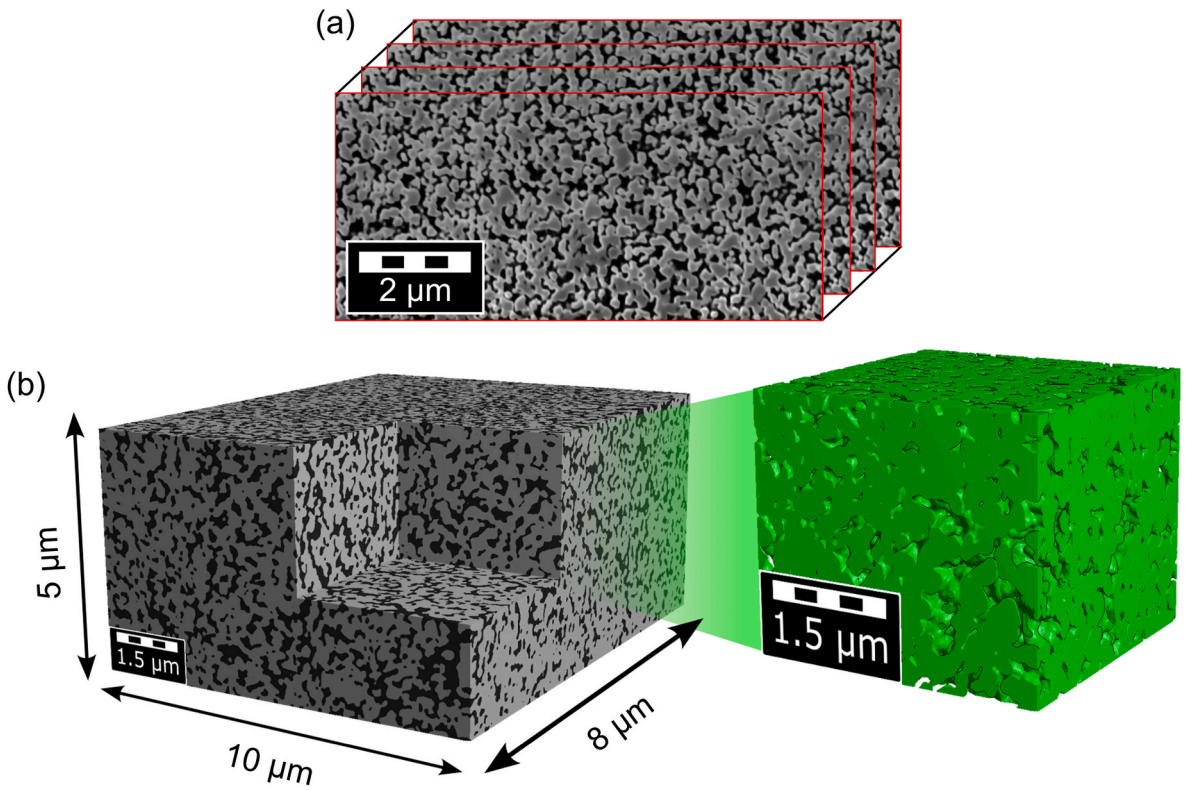

Fig. 1. (a) Consecutive recorded 2D images of the fuel electrode. The bright part represents the GDC and the black part the pores. (b) 3-D reconstruction of the volume of the fuel electrode.

ICD (InColumnDetector) detector. Due to the coarser GDC structure compared to the fuel electrode the pixel size of 22.5 nm is chosen here.

To quantify the GDC microstructures, images are initially aligned using an algorithm based on scale invariant feature transformation (SIFT) implemented in ImageJ [34]. A region of interest is then identified and cropped out using the software toolbox GeoDict 2023 [35]. Grey value gradients are removed. For noise removal, both an anisotropic diffusion filter as well as a non-linear means filtering provided in ImageJ and GeoDict, are used. Finally, cubic voxels are ensured by Tri-linear scaling. Due to strong contrast sustained by the infiltration with the carbon-based resin, grey value segmentation based on a hysteresis method, also known as region growing and provided through GeoDict, is applied.

The 3D reconstructed volume pictured in Fig. 1 (b) is evaluated for phase contents as well as GDC tortuosity. Phase contents are obtained following equation (1).

$$\varepsilon_{GDC} \quad \frac{Number\ of\ Voxels\ assigned\ to\ GDC}{Total\ number\ of\ voxels} \tag{1}$$

GDC tortuosity is obtained using the DiffuDict module in GeoDict 2023. To account for combined ionic and electronic conductivity, the Laplace equation is solved three times using a gradient of concentration in different space directions which yields the dimensionless diffusivity tensor D*.

$$\Delta c \quad 0 \tag{2}$$

This dimensionless quantity is only dependent on microstructure and does not contain any intrinsic material property. Using the volumetric phase content evaluated earlier we can calculate a tortuosity following equation (3) where ε_{GDC} is the phase content and $D_{x,y,z}$ is the dimensionless, relative diffusivity along the respective axis of the 3D reconstructed volume.

$$\tau_{GDC,x,y,z} \quad \frac{\varepsilon_{GDC}}{D_{x,y,z}} \tag{3}$$

In this case the z-axis represents the direction perpendicular to the plane of the electrode, sometimes referred to as the through-plane direction, whereas x and y represent the in-plane directions. Both directions are of interest because electrical conductivity is measured in-plane in the 4-point measurement and fuel electrode behavior is modeled in through-plane direction. All the parameters determined by 3D-reconstruction are given in Table 1.

3. DRT based modeling

3.1. Distribution of relaxation times

There are different ways to extract information of an impedance spectrum. A common way to represent and analyze an impedance spectrum is the Nyquist or Bode plot. For systems which include processes with large differences in their characteristic frequencies these methods are sufficient. But for more complex systems, where the characteristic frequencies of the processes are quite similar, an appropriate analysis without any a priori knowledge is not possible since the processes strongly overlap and cannot be separated [36].

One method to increase the extractable information of the measured impedance data without any a priori knowledge is to calculate their

Table 1
Parameters of 3-D reconstruction.

Parameter	Fuel electrode	Conductivity sample
$V_{rec}/\mu m^3$	380	2552
τ/-	1.31	1.57
ε/-	0.75	0.62
$A_{surface}/\mu m^2\ \mu m^{\ 3}$	10.7	–

distribution of relaxation times, which is used by many research groups [30,37–46]. The DRT has the advantage of a much higher frequency resolution in comparison to the raw impedance data. Therefore the separation of processes with quite similar time constants is much easier. The DRT calculation is based upon the fact that a valid impedance spectrum can be described by a simple equivalent circuit model based on a resistance for the ohmic losses R_{ohm} and a number of serial RC-elements for the polarization losses R_{pol} (equation (4) and (5)) [47]. Every RC-element represents a part of the polarization resistance $\gamma(\tau)\cdot R_{pol}$ at a specific time constant τ ranging from 0 to ∞ [1,3].

$$Z(\omega) \quad R_{ohm} + R_{pol}\cdot\int_0^{\infty}\frac{\gamma(\tau)}{1+j\omega\tau}d\tau \tag{4}$$

$$\int_0^{\infty}\gamma(\tau)d\tau \quad 1 \tag{5}$$

The criteria for the validity of an impedance spectrum are given in the Kramers-Kronig relations which connect real and imaginary part and confirm the time invariance, causality, linearity and finiteness [33,48]. This connection between the real and imaginary part is used in our implementation of the DRT calculation where only the real part of the impedance spectrum is used [3] since in spectra of fuel cells and electrolyzers the absolute value of the imaginary part is commonly much smaller and thus more strongly affected by noise.

For the actual calculation of the DRT of a given impedance a transformation of the second summand of equation (4) (polarization loss) to $\gamma(\tau)$ is necessary. This leads to a so-called ill-posed problem. In literature there are different approaches to solve this problem like Fourier transformation and the usage of digital filters and extrapolation [1] or approaches based on regularization methods [49,50]. Our approach is based on the Tikhonov-regularization described in Ref. [51] that was implemented in Matlab.

A correct selection of the regularization parameter is mandatory for an appropriate calculation of the DRT. If the regularization is too high, the peaks in the DRT are broadened, impeding the separation of neighboring peaks. If the regularization is too low, artificial peaks due to measurement noise occur in the spectrum. A sensitivity analysis, as it is shown in Figs. 2 and 3, is commonly used for determination of the regularization parameter. To enable the comparison of the DRTs of different spectra a similar regularization parameter is essential. In the following figures the distribution of relaxation times is plotted via a logarithmic x-axis displaying the frequency instead of the relaxation time. This approach is common as it enables a direct correlation with the measured values and impedance spectra in the Bode-plot.

3.2. Sensitivity analysis by EIS and DRT

Before setting up a physicochemical equivalent circuit model for an electrochemical cell, a deconvolution of the processes in the spectrum and a subsequent process assignment is necessary. This is done by a

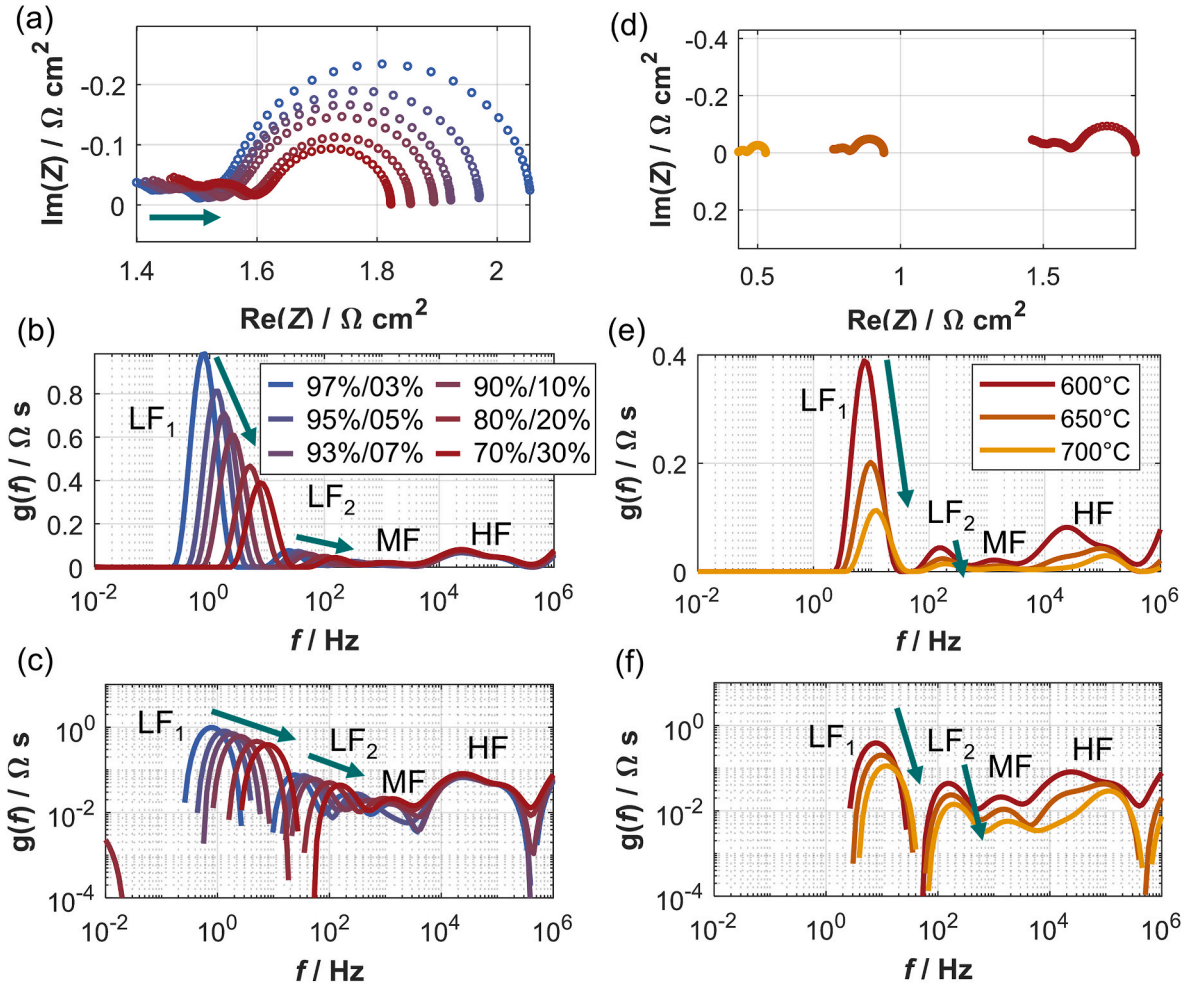

Fig. 2. Left: H_2/H_2O variation at constant temperature of 600 °C from 97 %/3 %–70 %/30 % H_2/H_2O. The Nyquist plot in (a) shows an increase of R_0 and a decrease of R_{pol} with higher steam content. The DRT (b, c) shows a decrease in peak height and an increase in peak frequency of the lower frequency peaks with higher steam content whereas the higher frequency part is minor dependent. Right: Variation of the temperature from 600 °C to 700 °C in 50 K steps at a constant H_2/H_2O ratio of 70 %/30 %. Every peak in the DRT is thermally activated as expected.

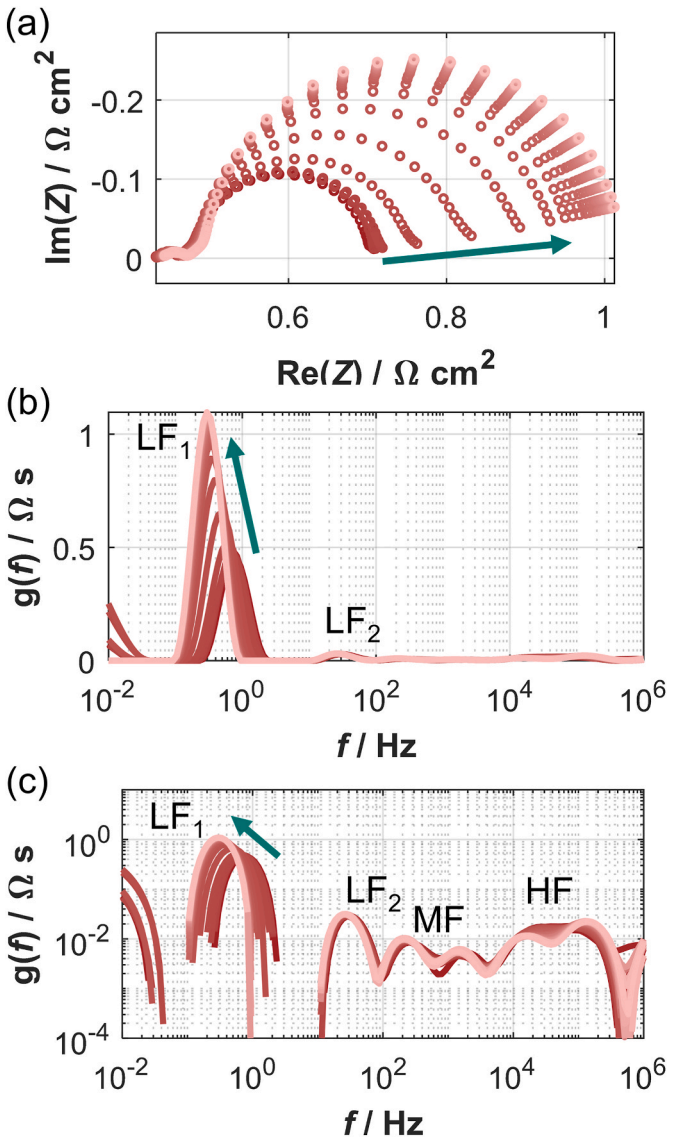

Fig. 3. Sulfur poisoning at 700 °C in 89 %/3 %/8 % $H_2/H_2O/N_2$ with 0.05 ppm H_2S over time. In the Nyquist-plot in (a) a strong increase of R_{pol} is visible. The DRT (b, c) visualizes that the major impact of the poisoning is allocated to LF_1. The other peaks and the ohmic resistance remain constant over time.

sensitivity analysis varying operating conditions [7] as temperature and gas composition.

Fig. 2(a–c) show a fuel gas variation at 600 °C from 97 %/03 % H_2/H_2O to 70 %/30 % H_2/H_2O. (a) shows the Nyquist plot, (b) the DRT in linear y-axis and (c) for a better visualization due to large differences in peak height in logarithmic scale. Please be aware that in the logarithmic scale the geometrical area under the DRT-curve is no longer corresponding to the polarization resistance of the peak. The peaks LF_1 and LF_2 are typically allocated to charge transfer reaction (or rather hydrogen adsorption and/or dissociation)/gas diffusion (~1 Hz) and to ionic transport in Ni/GDC fuel electrodes (~10–100 Hz) respectively [30,52–54]. The overlap of the gas diffusion and the charge transfer in the Ni/GDC is explained by the large chemical capacity of ceria which leads to a shift in the relaxation frequency [21,30,52,53,55,56]. Both LF-peaks decrease in resistance and increase in frequency with a higher steam content up to 30 %. The impact of steam to LF_1 is consistent with literature [52–55]. The observations of the peak between ~10 and 100 Hz differ between no impact [30,52,53] and a decrease in resistance as shown in Fig. 2 [55]. The peaks in the frequency range between LF_2 and 10 kHz show a comparable behavior to the LF peaks whereas the higher frequency part > 10 kHz is minor affected by the variation of the gas mixture. The peaks in the medium frequency range are rarely investigated since they have quite a small resistance compared to other peaks and are only visible in DRT and minor in the impedance spectrum. The impact of the high frequency peaks (>10 kHz) to the total polarization resistance increases with higher steam content up to 30 %, mainly due to the decrease of the LF-peaks. The ohmic resistance increases with higher steam content. An explanation would be that with a higher steam content in the fuel gas the pO_2 increases followed by a decrease of the electronic conductivity in the GDC (Fig. 7). Whereas the ionic resistance of 8YSZ dominates the ohmic resistance due to the thickness of 200 µm, the GDC fuel electrode contributes only a minor part (<50 mΩ cm^2) due to the thin layer (5 µm) as shown later in a simulation in Fig. 5 for 700 °C. Therefore, the change in ohmic resistance during the variation is rather small. In literature the ohmic resistance is less influenced by the gas mixture. In the Ni/GDC [55] this could be explainable by the electronic path through the Ni phase which should be pO_2 independent and in the GDC electrode [30] it might be due to high operation temperature of 900 °C and therefore high electronic conductivity of GDC.

Fig. 2(d–f) presents a temperature variation between 600 °C and 700 °C in 50 K steps at 30 % steam balanced in hydrogen. All the peaks including the ohmic resistance seem to be thermally activated as expected [30,52,53] and no separate peak for the gas diffusion is visible [53].

Fig. 3 pictures the impedance evolution during a sulfur poisoning experiment. At 700 °C in 89 %/3 %/8 % $H_2/H_2O/N_2$ 0.05 ppm H_2S were added in the fuel gas. The Nyquist-plot (a) shows a large increase of R_{pol} whereas R_0 stays constant. In the DRT (b, c) a strong increase of peak LF_1 is visible whereas the higher frequency peaks stay the same. This behavior is consistent with literature [29,56–58]. At frequencies much lower than 100 mHz an additional artificial peak is visible. The reason for this peak is the time variance during the poisoning [28,29].

With the information of these three variations a process assignment can be conducted as listed in Table 2. The peak LF_1 can be allocated to the charge transfer reaction due to the dependency on temperature, gas mixture and the impact of H_2S [29,56–58]. Sulfur poisons the electrocatalyst - in this case Nickel - and impedes the electrooxidation of hydrogen, which leads to a drastic increase of the charge transfer resistance as previously shown for Ni/YSZ and Ni/GDC fuel electrodes [15,57,59–62]. As already mentioned above the charge transfer reaction in Ni/GDC is in the same frequency range as the gas diffusion due to the large chemical capacity and is therefore not separable in the impedance/DRT [30,52,53,56], but relatively small in the electrolyte supported cell at intermediate temperatures [52]. The peaks in the medium frequency range (MF) between LF_2 and 10 kHz most probably describe bulk conductivities inside the electrode since the large main peak (LF_1) and the following smaller peaks feature a typical behavior of porous electrodes. This process assignment is supported by the recent publication of Uecker et al. who investigated a single phase GDC fuel electrode with Au-contact paste [30]. Peaks higher than 10 kHz are most probably losses related to the electrolyte [63–65] and the GDC/8YSZ-interface [66–68] since they show minor dependency on the gas mixture and no dependency on surface poisoning.

Based on the process assignment a physicochemically meaningful equivalent circuit model including a TLM for the GDC-electrode can be

Table 2
Peaks and processes in the impedance spectra and DRT.

Peak i	Dependencies	Physical process
LF_1	T, pH_2/pH_2O, H_2S	Charge transfer resistance + minor gas diffusion contribution
LF_2	T, pH_2/pH_2O	Transport processes in the electrode
MF	T, pH_2/pH_2O	Transport processes in the electrode
HF	T	Transport processes at the GDC/8YSZ-interface

developed.

3.3. Physicochemically meaningful TLM

Fig. 4 (a) illustrates the porous GDC electrode layer placed between the dense, oxygen ion conducting 8YSZ electrolyte substrate and the porous, solely electronically conducting Ni current collector layer. The electronic and ionic transport paths are connected via the charge transfer reactions at DPBs (GDC/pore-interfaces in the GDC-layer) and TPBs (triple phase boundary only at the GDC/Ni-interface). Most probably the existence of the Ni current collector layer leads to an interdiffusion of Ni into the porous GDC layer that activates the GDC surface, which could also explain the large impact of sulfur to the polarization resistance. We assume in this work that the charge transfer reaction occurs homogenously over the entire electrode area inside the GDC layer whereas the TPBs at the GDC/Ni-interface contribute only a minor part. To proof this assumption an electrode thickness variation will be performed in future work.

It has to be mentioned at this point that there are different notations in literature for the electrochemical reactions in ceria-based fuel electrodes. Generally, in the liquid electrochemistry the charge transfer defines the transition between the electronic path and the ionic path, where the actual electrochemical reaction takes place. In the Ni/YSZ fuel electrode the charge transfer from electronic path (Ni) to ionic path (YSZ) and the electrochemical reaction occur at the same spot at the triple phase boundary. Therefore, this whole reaction is named charge transfer. In the MIEC cathode (for instance LSCF) the electronic path and the ionic path are in the same material. The electrochemical reaction is defined as a surface exchange reaction on the MIEC which could be in a different spot than the charge transfer at the interface between LSCF cathode and GDC/YSZ electrolyte visible as different peaks in the impedance/DRT spectrum [13]. In ceria-based fuel electrodes different authors use different notations. Nielsen et al. [22] name the hydrogen electrooxidation in the investigated metal supported cell with GDC and Ni:GDC infiltration as the electrochemical reaction. Riegraf et al. [52] investigated a symmetrical Ni/GDC fuel electrode cell and describe the low frequency process as "a surface process at the GDC surface or TPB, probably the charge transfer process". Nenning et al. [21] describe the electrooxidation on the GDC surface of a Ni/GDC fuel electrode as the electrochemical reaction and surface oxygen exchange. Uecker et al. [30] investigated a single phase GDC fuel electrode contacted with an Au-paste. The low frequency process is named as the charge transfer at the GDC fuel electrode. In our work we use the same notation "charge transfer" as Uecker et al. [30] for the electrochemical reaction at the GDC surface.

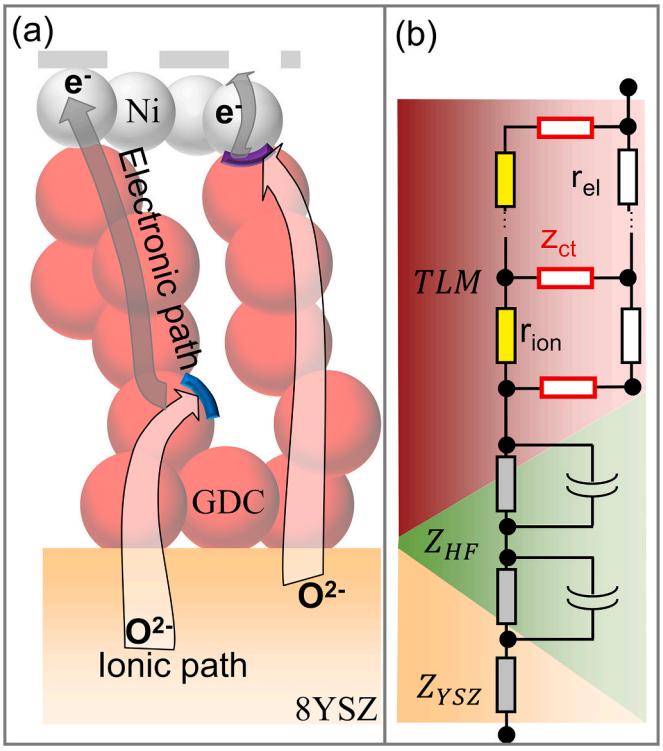

Fig. 4. (a) Schematic drawing of the electrochemistry of the investigated cell. The charge transfer at the DPB is colored in blue and the reaction at the TPB between Ni, GDC and gas phase in purple. (b) The equivalent circuit model consists of a two-channel transmission line model for the electrochemistry of the fuel electrode (red) in series to two RQ elements and one resistor for the description of the bulk losses related to the electrolyte (orange) and interface (green). (For interpretation of the references to color in this figure legend, the reader is referred to the Web version of this article.)

Commonly the electrochemistry of such porous electrodes is described by a transmission line model (Fig. 4 (b), red part). The general impedance function is given in equations (6) and (7) [9]. It includes the charge transfer resistance z_{ct} at the material-gas interphase and the losses occurring during ionic r_{ion} and electronic r_{el} transport. L describes the thickness of the electrode and κ the ratio between charge transfer resistance and resistances attributed to transport processes in the electrode. In this case we use κ instead of the often used "penetration depth" λ since a "penetration depth" is only meaningful if one of the transport paths is neglectable.

$$Z_{TLM} \quad \frac{r_{el}\cdot r_{ion}}{r_{el}+r_{ion}}\cdot\left(L+\frac{2\cdot\kappa}{sinh\left(\frac{L}{\kappa}\right)}\right)+\kappa\cdot\frac{r_{el}^2+r_{ion}^2}{r_{el}+r_{ion}}\cdot coth\left(\frac{L}{\kappa}\right) \tag{6}$$

$$\kappa \quad \left(\frac{z_{ct}}{r_{el}+r_{ion}}\right)^{1/2} \tag{7}$$

The electronic conductivity is – compared to other MIECs such as LSCF – minor and therefore the electronic resistance contribution r_{el} in the TLM is not neglectable as it is the case for the Gerischer element [13]. The resistances per length of both transport mechanisms are given in equations (8) and (9) whereas $\sigma_{i,GDC}$ is the bulk conductivity of GDC (i: electronic or ionic), A_{act} the active area of 1 cm^2, τ_{GDC} the tortuosity and ε_{GDC} the volume fraction.

$$r_{ion} \quad \frac{1}{\sigma_{ion,GDC}\cdot A_{act}}\cdot\frac{\tau_{GDC}}{\varepsilon_{GDC}} \tag{8}$$

$$r_{el} \quad \frac{1}{\sigma_{el,GDC}\cdot A_{act}}\cdot\frac{\tau_{GDC}}{\varepsilon_{GDC}} \tag{9}$$

The impedance of the charge transfer reaction is represented by equation (10). It should be noted that more complex equations considering the different elementary kinetic steps of such reactions can be included. In this case the simple and straightforward application of an RQ-element (resistance parallel to a constant phase element) was sufficient to obtain an excellent agreement between measurements and model.

$$z_{ct} \quad \frac{r_{ct}}{1+(j\,\omega\tau_{ct})^n} \tag{10}$$

The gas diffusion losses are not included in the TLM since in electrolyte supported cells the gas diffusion process is comparably small due to minor electrode thickness compared to an anode supported cell (ASC) [52,53]. With the approach by Grosselindemann et al. [53] a gas diffusion resistance contribution of less than 6 % of the total R_{pol} at 700 °C and 3 % steam in hydrogen could be determined (even smaller at lower temperatures and higher steam contents).

The losses related to the GDC/8YSZ-interface and the 8YSZ-electrolyte are modeled with two additional RQ-elements and a resistor

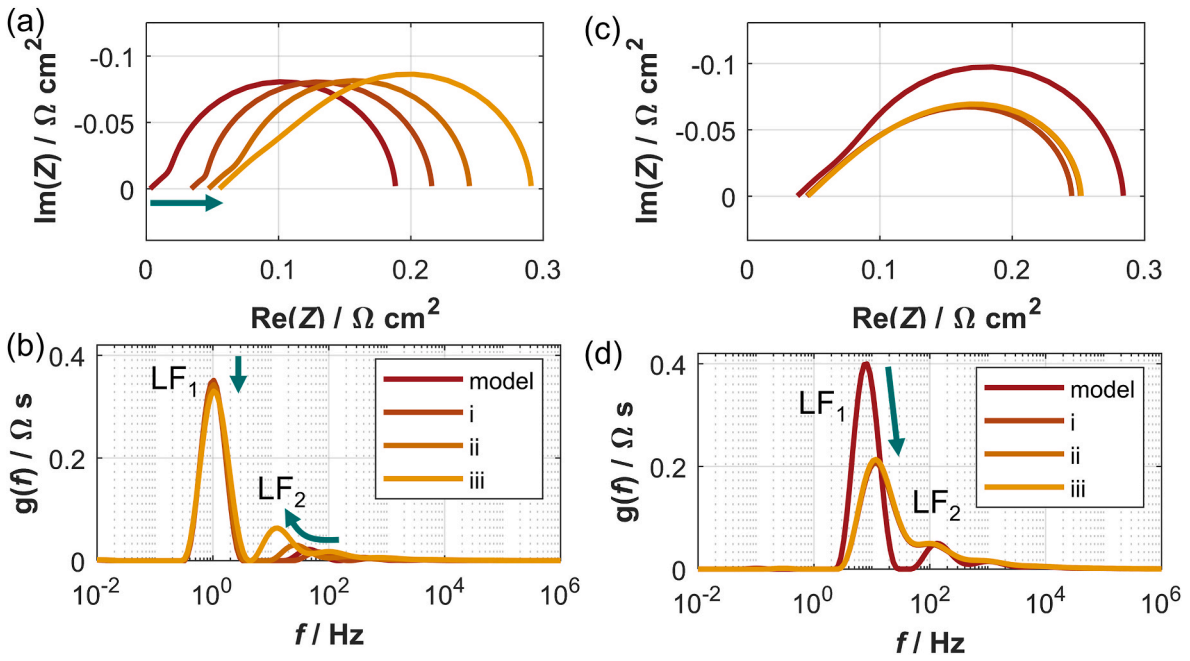

Fig. 5. (a, b) Simulation of a variation of transport resistances whereas the charge transfer is kept constant. The first impedance (red) corresponds to the electrode at 700 °C in 97 %/03 % H_2/H_2O. The variation of κ leads in the Nyquist plot to an increase of the ohmic resistance and to a transformation to a Gerischer shape. In the DRT an increase of peak LF_2 is visible. (c, d) Variation of r_{ct} and r_{ion} by the same factor whereas r_{el} stays constant visualize the ambiguity of the TLM if $L \gg \kappa$ and $r_{el} \ll r_{ion}$. The first impedance (red) corresponds to the electrode at 600 °C in 70 %/30 % H_2/H_2O. (For interpretation of the references to color in this figure legend, the reader is referred to the Web version of this article.)

respectively.

$$Z_{RQ} \quad \frac{R}{1 + (j\,\omega\tau_{RQ})^n} \tag{11}$$

3.4. Simulation study for the two-channel TLM

Since the two-channel transmission line model with a non-negligible electronic path is not common in the field of SOCs a simulation study was performed. In the figures only the impedance/DRT of the transmission line model is displayed, the additional elements for GDC/8YSZ-interface and 8YSZ-electrolyte are not considered.

In Fig. 5 (a, b) the impact of the electronic and ionic charge transport resistance on the impedance spectrum/DRT is shown. The charge transfer resistance r_{ct} is kept constant during all simulations to reveal the impact of electronic and ionic transport only. It should be noted that in the real electrode r_{ct} is strongly depending on the fuel gas composition, as visible in Fig. 2 (a - c). The starting values for the individual parameters correspond to the investigated electrode at 700 °C in 97 %/03 % H_2/H_2O (first impedance, red). The chosen electronic and ionic conductivities are marked as orange/blue dots in Fig. 7 (d). They correspond to steam contents of 3 %, 95 %, 99 % and >99 % balanced with hydrogen. The strong increase of the electronic resistance r_{el} and the slight increase of the ionic resistance r_{ion} (from red to yellow) result in an increased ohmic resistance (Fig. 5 a) as it was measured in Fig. 2 (a). The shape of the spectrum is changing from a depressed semicircle with some kink at high frequencies to a Gerischer type impedance. This is related to the difference in κ which exceeds the GDC electrode thickness of $L \quad 5\,\mu m$ in the red spectrum and is lower in the yellow spectrum respectively (Table 3). In the DRT such change in electronic and/or ionic conductivities mainly affects the peak LF_2. With increasing resistance an increase of the peak height and a shift to lower frequencies is visible. The peak LF_1, which according to the sensitivity analysis is attributed to the charge transfer reactions, is decreasing slightly.

Fig. 5 (c, d) pictures a systematic variation of r_{ct} and r_{ion} whereas r_{el} stays constant. The first spectrum in red corresponds to the electrode at 600 °C in 70 %/30 % H_2/H_2O. With a decrease in r_{ct} and an increase in r_{ion} by the same factor of 10 (Table 4) the impedance and DRT changes (model → i). A large influence is visible in the peak LF_1 whereas the impact on LF_2 is minor. The further decrease in r_{ct} combined with an appropriate increase in r_{ion} lead to no further changes in impedance and DRT (i, ii, iii). The explanation can be found in the general impedance function of the transmission line model in equation (6). If κ is much lower than L the impedance function can be simplified to equation (12).

$$Z_{TLM}(L \gg \kappa) \quad \frac{r_{el} \cdot r_{ion}}{r_{el} + r_{ion}} \cdot L + \kappa \cdot \frac{r_{el}^2 + r_{ion}^2}{r_{el} + r_{ion}} \tag{12}$$

If one of the transport resistances (in this example r_{el}) is neglectable equation (12) can be further simplified to a simple multiplication of z_{ct} and r_{ion}. This simplification can be applied in the simulation in Fig. 5 (c, d) from spectrum i to iii. The ambiguity of the transmission line model [16] is clearly visible and will be further investigated in the following

Table 3
TLM parameters of variation of transport resistances (Fig. 5 a, b).

TLM parameter	model	i	ii	iii
r_{ct}/Ω µm	0.9	0.9	0.9	0.9
r_{ion}/mΩ µm^{-1} (pH_2O)	9.6 (3 %)	12.6 (95 %)	12.6 (99 %)	12.6 (>99 %)
r_{el}/mΩ µm^{-1} (pH_2O)	0.6 (3 %)	13.1 (95 %)	29.8 (99 %)	59.6 (>99 %)
κ/µm	9.4	5.9	4.6	3.5
L/µm	5.3	5.3	5.3	5.3

Table 4
TLM parameters of variation of r_{ct} and r_{ion} (Fig. 5 c, d).

TLM parameter	model	i	ii	iii
r_{ct}/Ω µm	1.07	0.107	0.011	0.001
r_{ion}/Ω µm^{-1}	0.04	0.4	4.02	40.2
r_{el}/mΩ µm^{-1}	8.6	8.6	8.6	8.6
κ/µm	4.67	0.51	0.05	0.005
L/µm	5.3	5.3	5.3	5.3

where a parametrization of the model without any further knowledge except of the impedance spectrum is performed.

3.5. Model parametrization by straightforward CNLS/DRT fitting

For the parameterization of equivalent circuit models, often the model is straightforward fitted to the measured spectra. In this fitting procedure the DRT can support an accurate fitting and ensure appropriate relaxation frequencies for the different processes. Starting values are estimated from impedance spectra and DRT without considering externally measured parameters. Fig. 6 shows that a number of different model parameter sets (Table 5) are able to represent the measured spectrum with an excellent accuracy. Despite of the fact that some parameters are varied significantly or were even exchanged, neither the spectra nor the DRTs show any significant differences. Thus the determined model parameters are not physicochemically meaningful even if they are able to reproduce the measured spectrum. This visualizes that a direct fitting of the transmission line model is impossible as discussed for Ni/YSZ fuel electrodes in Ref. [16].

Due to the symmetry of the TLM, an exchange of the resistance values r_{ion} and r_{el} of both transport paths does not affect the result at all. This is shown in the first scenario. The TLM fit in green shows a good agreement (error < 0.15 %, f 1 Hz … 10 kHz) with the measurement data in grey for both model parameter sets (i, i.2). The relative error between measurement and TLM fit is calculated according to equations (13) and (14).

$$\Delta Z'(\omega) \quad \frac{Z'_{fit}(\omega) \quad Z'_{meas}(\omega)}{|Z_{meas}(\omega)|} \tag{13}$$

$$\Delta Z''(\omega) \quad \frac{Z''_{fit}(\omega) \quad Z''_{meas}(\omega)}{|Z_{meas}(\omega)|} \tag{14}$$

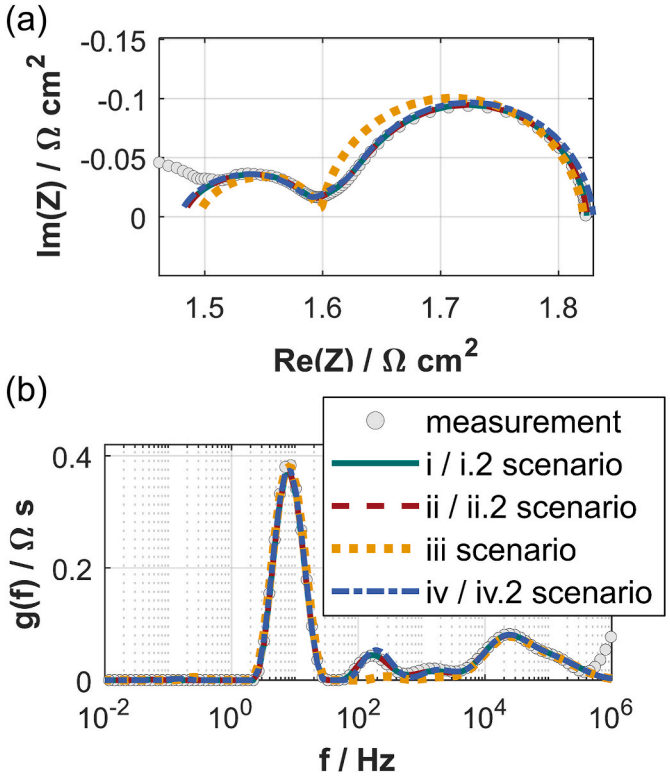

Fig. 6. Transmission line model fits and the corresponding measurement at 600 °C in 70 %/30 % H_2/H_2O (grey). A direct fitting with open model parameters leads to different parameter sets (Table 5) which result in comparable impedance/DRT. (a) shows the Nyquist-Plot and (b) the DRTs.

It is further shown that a multiplication of r_{ct}/L and a division of r_{ion}/r_{el} by the same factor leads to the identical impedance pictured in red as the 2nd scenario (ii, ii.2). The impedance and the DRT show also an excellent agreement (error < 0.15 %, f 1 Hz … 10 kHz) with the measurement data. This connection is valid if κ is lower than L as shown in the previous section.

Scenario iii and iv show simplified models. In iii the charge transport resistances r_{ion} and r_{el} in the TLM are neglected and set to 0. In this model there is, apart from the high frequency processes, basically one RQ element from the charge transfer impedance z_{ct} left. The fitting result shows a significant deviation in the frequency range between 50 Hz and 3 kHz as charge transport in the GDC is neglected. Considering the low overall contribution of the charge transport, this leads to an error < 1.3 % (f 1 Hz … 10 kHz) only. As shown in Ref. [16] a significantly better agreement can be achieved if 2 to 3 RQ elements are used. Despite of an excellent fit the obtained parameters are not meaningful.

In the fourth scenario (iv, iv.2) one of the transport paths is expected to show no significant loss and therefore r_{ion} and r_{el} are alternatively set to 0. The fitting result is much better compared to the 3rd scenario, but show still some deviations in the peak LF_2 (error < 0.3 %, f 1 Hz … 10 kHz).

This reinforces that the application of the more complex two-channel transmission line model is necessary combined with an independent experimental parameterization is mandatory for a meaningful interpretation of impedance spectra of the investigated GDC electrode.

3.6. Advanced model parametrization

As shown in the previous section (scenario 1 and 2), the measured spectra can be fitted accurately with different parameter sets. This is due to the exchangeability of ionic and electronic conduction as well as the interaction of conduction and charge transfer enabling similar spectra and DRTs despite of different TLM-parameters.

For a meaningful TLM-parameterization at least a part of the parameters have to be determined independently by different measurement and analysis methods. As it is much more difficult to determine the charge transfer resistance by means of appropriate model electrodes [71, 72], the effective electronic and ionic conductivity of the porous GDC-layer considering the impact of its microstructure is determined. In comparison to zirconia based electrolytes – exhibiting a purely ionic, pO_2-independent conductivity – the conductivity of the mixed conducting ceria is pO_2-dependent and furthermore composed of ionic and electronic contributions. Thus pO_2- and temperature-dependency of ionic and electronic conductivity have to be determined for model parameterization.

Fig. 7 includes all the steps for the determination of the conductivity parameters used in the TLM. Fig. 7 (a) pictures a cross section of the GDC layer applied on a MgO substrate. The measured values of the porous GDC layer (Fig. 7 b) represent the effective conductivity. As the microstructure of the GDC layer on the MgO-substrate differs from that used in the symmetrical cells, 3-D reconstructions as exemplary shown in Fig. 1 for the fuel electrode is necessary in order to determine the microstructural parameters. The microstructural parameters and the geometry are given in Table 1. After correcting the measured data with the microstructural parameters (equation (15)), the bulk conductivity is received which is in good agreement with literature data.

$$\sigma_{bulk} \quad \sigma_{effective} \cdot \frac{\tau_{GDC}}{\varepsilon_{GDC}} \tag{15}$$

Fig. 7 (c) pictures the comparison of the different data sets (literature data extracted by software OriginLab) at 700 °C. The measured bulk conductivity is colored in blue. Additionally, a technically relevant operation window between 1 % and 99 % steam in hydrogen is marked between two orange dotted lines.

For separation of the ionic and electronic conductivity an approach published by Wang et al. [69] is used. This approach uses the relation

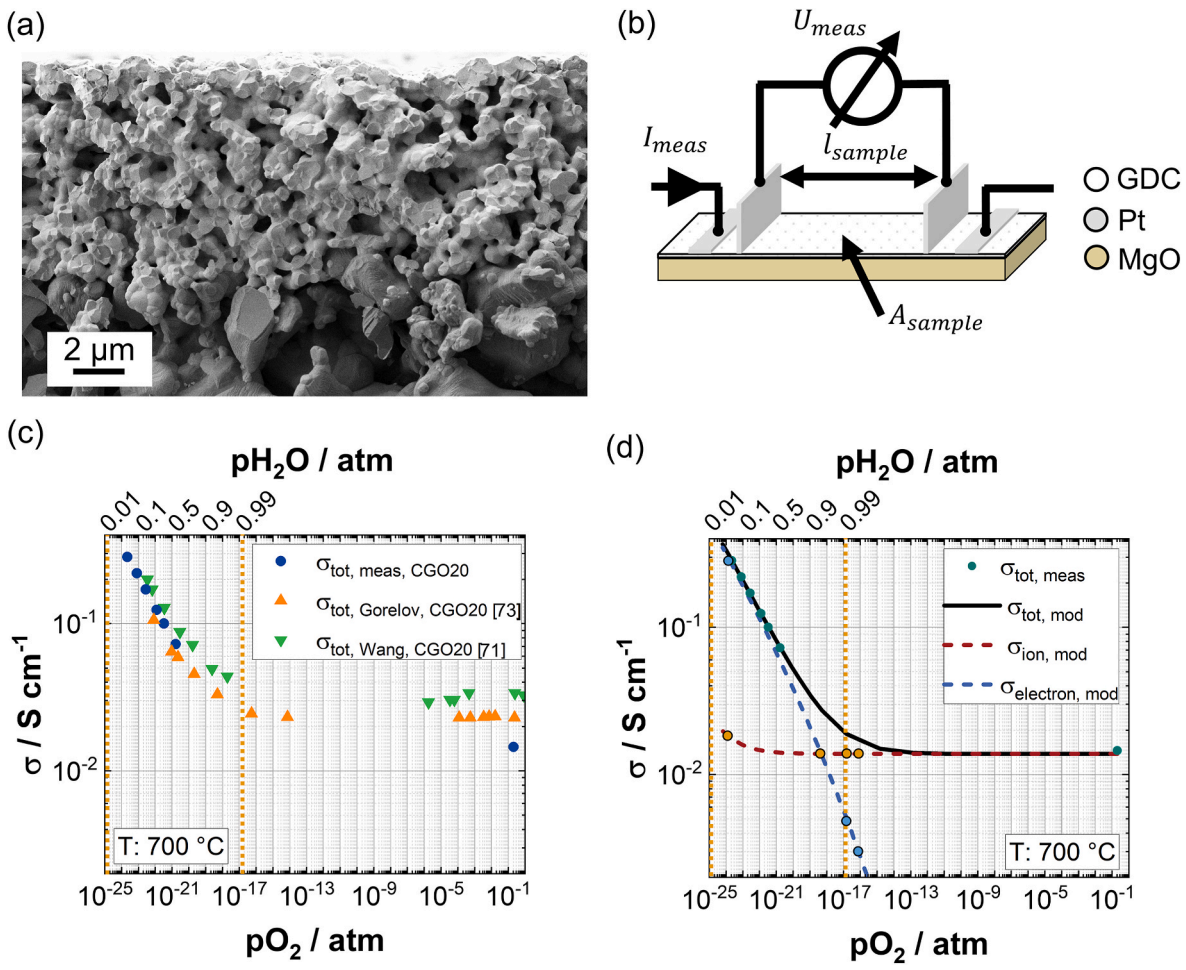

Fig. 7. (a) Cross section of a porous GDC layer applied on a MgO substrate. (b) Setup of the conductivity measurement. The current input consists of a sintered Pt-electrode (1050 °C) and a 0.2 mm Pt-wire. The voltage is measured between Pt-electrodes. (c) Comparison of measured bulk conductivity (blue) with literature data [69,70]. (d) Measured conductivity (green), modeled bulk conductivity (black), calculated ionic (red) and electronic (blue) conductivity over pO_2/pH_2O. The technically relevant operation window from 1 % steam to 99 % steam in hydrogen is marked between two orange dotted lines. Blue/orange dots represent the electronic/ionic conductivity values used for the simulation study in Fig. 5 (a, b). (For interpretation of the references to color in this figure legend, the reader is referred to the Web version of this article.)

Table 5
TLM parameter of every scenario of Fig. 6.

TLM parameter	i	i.2	ii	ii.2	iii	iv	iv.2
r_{ct}/Ω µm	1.04	1.04	2.08	2.08	1.6	0.98	0.98
r_{ion}/mΩ µm ^{1}	45	15.8	22.5	7.9	0	0	26.0
r_{el}/mΩ µm ^{1}	15.8	45	7.9	22.5	0	26.0	0
κ/µm	4.1	4.1	8.3	8.3	–	6.1	6.1
L/µm	5.3	5.3	10.6	10.6	7.4	4.75	4.75

between the non-stoichiometry/oxygen vacancies $[V_0^{\bullet\bullet}]$ and the conductivity σ (eq. (16)) in order to separate the electronic and ionic conductivity from the total conductivity. Further information can be found in Ref. [69].

$$\sigma_{ion} \quad 2 \cdot e \cdot \mu_{ion} \cdot [V_0^{\bullet\bullet}] \tag{16}$$

The non-stoichiometry data which is used in this work origins from a 10 mol.% gadolinia doped ceria sample [73], because in literature no data for GDC20 in the investigated temperature range is available. This needs to be considered for the further investigations since it could have an impact on the conductivity parameters used in the model.

Fig. 7 (d) shows the measured bulk conductivity in green and the fitted total conductivity in black as well as the ionic (red) and electronic conductivity (blue) calculated by the approach of Wang [69]. In reducing atmosphere, the ionic conductivity increases only slightly whereas the electronic conductivity rises strongly. The orange and blue dots represent conductivity values which are used in the simulation study in Fig. 5 (a, b).

3.7. Model fit

The TLM fit including the advanced parametrization shows an excellent agreement between model fit (green) and measurement data (grey circles) exemplary shown for the highest and the lowest investigated pH_2O at 600 °C in Fig. 8. (a, d) shows the Nyquist plot and (b, e) the DRT.

The relative error of imaginary and real part is pictured in (c, f) which is in both cases in the range of $< \pm 1$ % in the investigated frequency range from 100 mHz to 300 kHz. The excellent agreement between measurement and parameterized TLM is a basis for further cell understanding and can also be used for cell development.

For verifying the extracted charge transfer resistance, it is compared to literature values. To our knowledge no physicochemical analysis with a transmission line model is done for the investigated kind of GDC cell. Nenning et al. [21] fitted in a Ni/GDC fuel electrode applied in an electrolyte supported cell a resistance for the electrochemical reaction of 70 µΩ cm^3 at 650 °C. Since the given value is related to the volume we converted the resistance to compare the value with our results. With

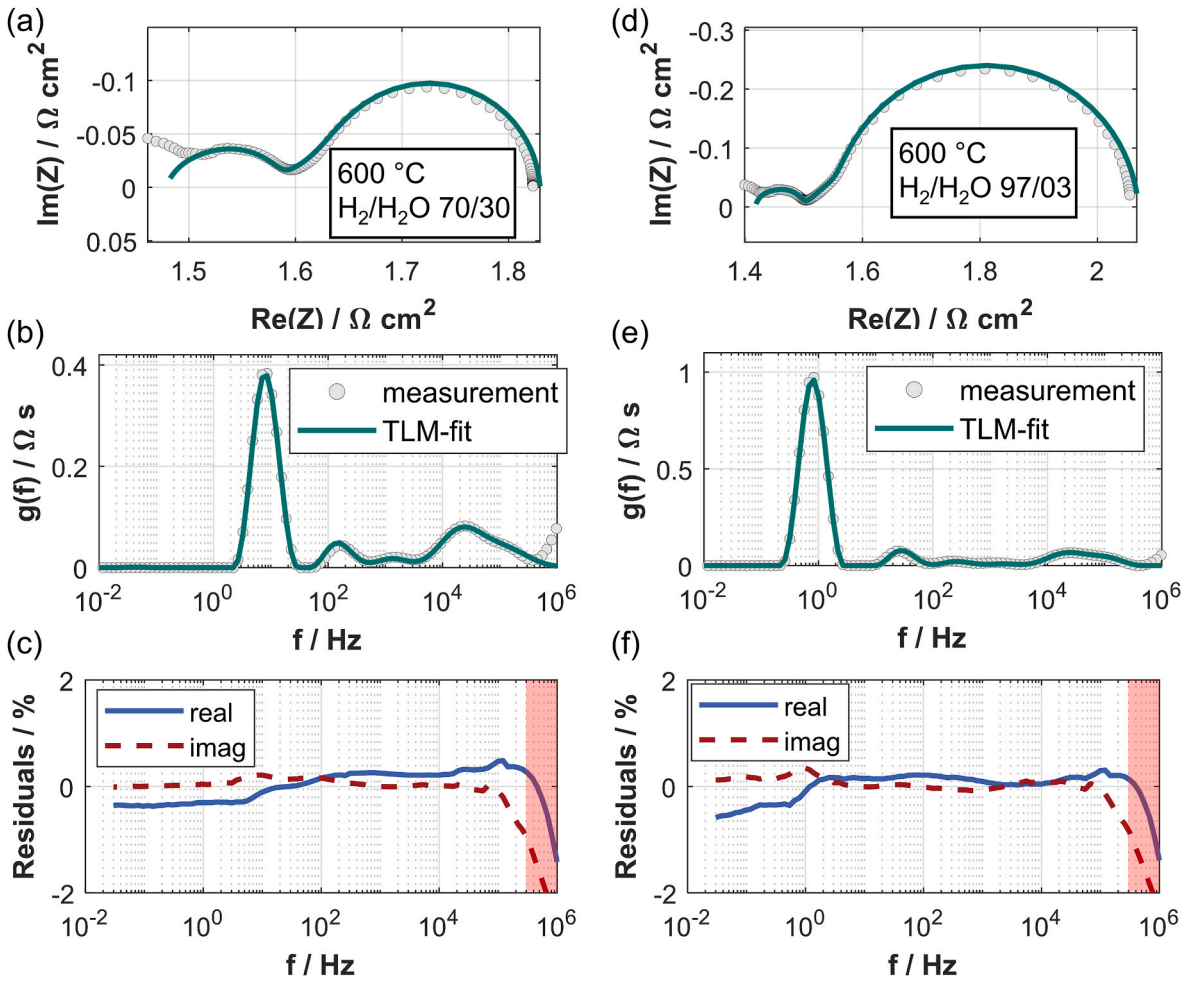

Fig. 8. Quality of the model fit at 600 °C in different operation conditions (left: 30 % steam in hydrogen, right: 3 % steam) pictured as Nyquist plot (a, d) and DRT (b, e). The green line represents the fit whereas the grey circles represent the measured data. The relative error is in both cases of the real part and the imaginary part < 1 % (100 mHz < f < 300 kHz). (For interpretation of the references to color in this figure legend, the reader is referred to the Web version of this article.)

0.87 Ω µm it is about 60 % higher than the value extracted from our GDC fuel electrode (0.54 Ω µm) operated in a similar atmosphere (70 %/30 % H_2/H_2O). There could be plenty of reasons like a higher GDC surface area, which is in our GDC electrode twice the area (10.7 $\mu m^2\ \mu m^{-3}$) compared to Ref. [21]. The performance improvement between a Ni/GDC electrode and our GDC fuel electrode is shown in a recent publication [28]. Compared to the two fuel electrodes investigated by Nielsen et al. [22] our electrode is in the range of the MSC infiltrated with Ni:GDC, but has a higher performance than the GDC infiltrated cell at 650 °C in 97 %/3 % H_2/H_2O with 1.50 Ω µm. The improvement in performance of ceria-based fuel electrodes by infiltration of Ni nanoparticles is well known and shown in different publications [28,29,54,74].

4. Conclusions

In this study we developed and parametrized a physicochemically meaningful transmission line model for a single phase GDC fuel electrode with a single phase Ni-contact layer. We showed that for impedance modeling, DRT-analysis and subsequent CLNS-fitting are insufficient to achieve a physicochemically meaningful TLM-parameterization. The mathematical structure of the transmission line impedance equation enables a proper reproduction of measured spectra despite of strongly differing model parameter sets. For a correct parameterization at least a few parameters of the model have to be determined in advance. Methods like 4-point dc measurements and focused ion beam-tomography were performed in order to obtain the conductivity of the GDC-phase and microstructural parameters like tortuosity and volume fractions. The pre-parametrized transmission line model was fitted to measured spectra, enabling access to further material specific parameters as the charge transfer resistance at the GDC-surface.

The parameterized model shows an excellent agreement with measured impedance spectra in a wide range of operating conditions. It can be applied in model based cell development and enables the analysis of performance and durability of full cells with ceria based anodes.

The application of the TLM-approach to Ni/GDC cermet electrodes is in general possible but two challenges have to be considered. The charge transfer is no longer limited to the GDC surface (double phase boundary) but the impact of the TPB's has to be considered. Furthermore, in case of a continuous Ni-matrix, the electronic path in the layer can be assumed to be short circuited ($\sigma_{Ni} \gg \sigma_{GDC}$). Due to the electronic conduction in the ceria phase a continuous Ni-matrix is not essential for Ni/GDC cermet electrodes. If the Ni-matrix is locally interrupted due to the electrode manufacturing process or Ni-agglomeration, the effective electronic conductivity cannot be determined as done in our approach and it will be much more challenging to obtain electronic and ionic conductivity of the electrode layer. For the application in different, more advanced cell concepts as fuel electrode or metal supported cells, there is the need to add an additional Warburg element describing the gas diffusion in the substrate.

CRediT authorship contribution statement

F. Kullmann: Methodology, Software, Validation, Formal analysis, Investigation, Writing – original draft, Writing – review & editing, Visualization, Project administration. **M. Mueller:** Software. **A. Lindner:** Investigation, Visualization, Writing – original draft. **S. Dierickx:** Conceptualization, Writing – review & editing. **E. Mueller:** Investigation. **A. Weber:** Conceptualization, Supervision, Funding acquisition, Writing – original draft, Writing – review & editing.

Declaration of competing interest

The authors declare that they have no known competing financial interests or personal relationships that could have appeared to influence the work reported in this paper

Data availability

Data will be made available on request.

Acknowledgments

We gratefully acknowledge funding from the German Federal Ministry of Education and Research (BMBF) within the WirLebenSOFC project No.: 03SF0622E. The authors thank Luis Salamon for the assistance in the laboratory, Annette Schucker for the assistance in FIB/SEM sample preparation and measurements and Stefan Henneck for fabricating the MgO substrates. Werner Herzhof and Alexander Schwiers, Forschungszentrum Jülich, IEK-1 are gratefully acknowledged for preparing and supplying the GDC pastes.

References

[1] H. Schichlein, A.C. Müller, M. Voigts, A. Krügel, E. Ivers-Tiffée, Deconvolution of electrochemical impedance spectra for the identification of electrode reaction mechanisms in solid oxide fuel cells, J. Appl. Electrochem. 32 (2002) 875, https://doi.org/10.1023/A:1020599525160.

[2] B.A. Boukamp, A nonlinear least square fit procedure for analysis of immittance data of electrochemical systems, Solid State Ionics 20 (1986) 31–44, https://doi.org/10.1016/0167-2738(86)90031-7.

[3] V. Sonn, A. Leonide, E. Ivers-Tiffée, Combined deconvolution and CNLS fitting approach applied on the impedance response of technical Ni/8YSZ cermet electrodes, J. Electrochem. Soc. 155 (2008) B675–B679, https://doi.org/10.1149/1.2908860.

[4] J. Illig, M. Ender, A. Weber, E. Ivers-Tiffée, Modeling graphite anodes with serial and transmission line models, J. Power Sources 282 (2015) 335–347, https://doi.org/10.1016/j.jpowsour.2015.02.038.

[5] M. Heinzmann, A. Weber, E. Ivers-Tiffée, Impedance modelling of porous electrode structures in polymer electrolyte membrane fuel cells, J. Power Sources 444 (2019), 227279, https://doi.org/10.1016/j.jpowsour.2019.227279.

[6] A. Weber, Impedance analysis of porous electrode structures in batteries and fuel cells, Technisches Messen 88 (2021) 1–16, https://doi.org/10.1515/teme-2020-0084.

[7] A. Leonide, V. Sonn, A. Weber, E. Ivers-Tiffée, Evaluation and modeling of the cell resistance in anode-supported solid oxide fuel cells, J. Electrochem. Soc. 155 (2008) B36–B41, https://doi.org/10.1149/1.2801372.

[8] J. Euler, W. Nonnenmacher, Stromverteilung in porosen elektroden, Electrochim. Acta 2 (1960) 268–286, https://doi.org/10.1016/0013-4686(60)80025-4.

[9] J. Bisquert, G. Garcia-Belmonte, F. Fabregat-Santiago, A. Compte, Anomalous transport effects in the impedance of porous film electrodes, Electrochem. Commun. 1 (1999) 429–435, https://doi.org/10.1016/S1388-2481(99)00084-3.

[10] N. Ogihara, Y. Itou, T. Sasaki, Y. Takeuchi, Impedance spectroscopy characterization of porous electrodes under different electrode thickness using a symmetric cell for high-performance lithium-ion batteries, J. Phys. Chem. C 119 (2015) 4612–4619, https://doi.org/10.1021/jp512564f.

[11] C. Gerling, M. Hanauer, U. Berner, K. Andreas Friedrich, Full factorial in situ characterization of ionomer properties in differential PEM fuel cells, J. Electrochem. Soc. 168 (2021), 084504, https://doi.org/10.1149/1945-7111/ac1812.

[12] S. Touhami, J. Mainka, J. Dillet, S.A.H. Taleb, O. Lottin, Transmission line impedance models considering oxygen transport limitations in polymer electrolyte membrane fuel cells, J. Electrochem. Soc. 166 (2019) F1209–F1217, https://doi.org/10.1149/2.0891915jes.

[13] S.B. Adler, J.A. Lane, B.C.H. Steele, Electrode kinetics of porous mixed-conducting oxygen electrodes, J. Electrochem. Soc. 143 (1996) 3554–3564, https://doi.org/10.1149/1.1837252.

[14] J. Nielsen, P. Hjalmarsson, M.H. Hansen, P. Blennow, Effect of low temperature in-situ sintering on the impedance and the performance of intermediate temperature solid oxide fuel cell cathodes, J. Power Sources 245 (2014) 418–428, https://doi.org/10.1016/j.jpowsour.2013.06.067.

[15] S. Dierickx, T. Mundloch, A. Weber, E. Ivers-Tiffée, How sulfur tolerance of two-layered Ni/YSZ anodes is governed by variations in microstructure and thickness, ECS Trans. 78 (2017) 1273–1284, https://doi.org/10.1149/07801.1273ecst.

[16] S. Dierickx, J. Joos, A. Weber, E. Ivers-Tiffée, Advanced impedance modelling of Ni/8YSZ cermet anodes, Electrochim. Acta 265 (2018) 736–750, https://doi.org/10.1016/j.electacta.2017.12.029.

[17] E.C. Shin, J. Ma, P.A. Ahn, H.H. Seo, D.T. Nguyen, J.S. Lee, Deconvolution of four transmission-line-model impedances in Ni-YSZ/YSZ/LSM solid oxide cells and mechanistic insights, Electrochim. Acta 188 (2016) 240–253, https://doi.org/10.1016/j.electacta.2015.11.118.

[18] R. Mohammadi, M. Søgaard, T. Ramos, M. Ghassemi, M.B. Mogensen, Electrochemical impedance modeling of a solid oxide fuel cell anode, Fuel Cell. 14 (2014) 645–659, https://doi.org/10.1002/fuce.201300292.

[19] J. Nielsen, J. Hjelm, Impedance of SOFC electrodes: a review and a comprehensive case study on the impedance of LSM:YSZ cathodes, Electrochim. Acta 115 (2014) 31–45, https://doi.org/10.1016/j.electacta.2013.10.053.

[20] E.C. Shin, P.A. Ahn, H.H. Seo, D.T. Nguyen, S.D. Kim, S.K. Woo, J.H. Yu, J.S. Lee, Pinning-down polarization losses and electrode kinetics in cermet-supported LSM solid oxide cells in reversible operation, Solid State Ionics 277 (2015) 1–10, https://doi.org/10.1016/j.ssi.2015.04.009.

[21] A. Nenning, C. Bischof, J. Fleig, M. Bram, A.K. Opitz, The relation of microstructure, materials properties and impedance of SOFC electrodes: a case study of Ni/GDC anodes, Energies 13 (2020) 987, https://doi.org/10.3390/en13040987.

[22] J. Nielsen, T. Klemenso, P. Blennow, Detailed impedance characterization of a well performing and durable Ni:CGO infiltrated cermet anode for metal-supported solid oxide fuel cells, J. Power Sources 219 (2012) 305–316, https://doi.org/10.1016/j.jpowsour.2012.07.031.

[23] D. Udomsilp, J. Rechberger, R. Neubauer, C. Bischof, F. Thaler, W. Schafbauer, N. H. Menzler, L.G.J. de Haart, A. Nenning, A.K. Opitz, O. Guillon, M. Bram, Metal-supported solid oxide fuel cells with exceptionally high power density for range extender systems, Cell Rep Phys Sci 1 (2020), https://doi.org/10.1016/j.xcrp.2020.100072.

[24] M. Gerstl, A. Hutterer, J. Fleig, M. Bram, A.K. Opitz, Model composite microelectrodes as a pathfinder for fully oxidic SOFC anodes, Solid State Ionics 298 (2016) 1–8, https://doi.org/10.1016/j.ssi.2016.10.013.

[25] M. Mogensen, T. Lindegaard, U.R. Hansen, G. Mogensen, Physical properties of mixed conductor solid oxide fuel cell anodes of doped CeO2, J. Electrochem. Soc. 141 (1994) 2122–2128, https://doi.org/10.1149/1.2055072.

[26] M. Mogensen, J.J. Bentzen, Oxidation of methane on oxide electrodes at 800–1000°C, Proc. Electrochem. Soc. (1989) 99–110, https://doi.org/10.1149/198911.0099pv. PV 1989-11.

[27] B.C.H. Steele, P.H. Middleton, R.A. Rudkin, Material science aspects of SOFC technology with special reference to anode development, Solid State Ionics 40–41 (1990) 388–393, https://doi.org/10.1016/0167-2738(90)90364-W.

[28] F. Kullmann, A. Schwiers, M. Juckel, N.H. Menzler, A. Weber, Influence of microstructure on the sulfur tolerance of ceria-based anodes in low temperature SOFC, ECS Trans. 111 (2023) 1013, https://doi.org/10.1149/11106.1013ecst.

[29] A. Weber, S. Dierickx, N. Russner, E. Ivers-Tiffée, Sulfur poisoning of Ni-based SOFC-anodes – short and long term behavior, ECS Trans. 77 (2017) 141–147, https://doi.org/10.1149/07710.0141ecst.

[30] J. Uecker, I.D. Unachukwu, V. Vibhu, I.C. Vinke, R.A. Eichel, L.G.J. Bert de Haart, Performance, electrochemical process analysis and degradation of gadolinium doped ceria as fuel electrode material for solid oxide electrolysis cells, Electrochim. Acta 452 (2023), 142320, https://doi.org/10.1016/j.electacta.2023.142320.

[31] A. Nenning, M. Holzmann, J. Fleig, A.K. Opitz, Excellent kinetics of single-phase Gd-doped ceria fuel electrodes in solid oxide cells, Mater Adv 2 (2021) 5422–5431, https://doi.org/10.1039/d1ma00202c.

[32] D. Klotz, A. Weber, E. Ivers-Tiffée, Practical guidelines for reliable electrochemical characterization of solid oxide fuel cells, Electrochim. Acta 227 (2017) 110–126, https://doi.org/10.1016/j.electacta.2016.12.148.

[33] M. Schonleber, D. Klotz, E. Ivers-Tiffée, A method for improving the robustness of linear kramers-kronig validity tests, Electrochim. Acta 131 (2014) 20–27, https://doi.org/10.1016/j.electacta.2014.01.034.

[34] T. Lindeberg, Scale invariant feature transform, Scholarpedia 7 (2012), 10491, https://doi.org/10.4249/scholarpedia.10491.

[35] GeoDict software, Release 2023 from Math2Market GmbH, Germany. (n.d.).. https://www.geodict.com.

[36] E. Ivers-Tiffée, A. Weber, Evaluation of electrochemical impedance spectra by the distribution of relaxation times, J. Ceram. Soc. Jpn. 125 (2017) 193–201, https://doi.org/10.2109/jcersj2.16267.

[37] I.D. Unachukwu, V. Vibhu, I.C. Vinke, R.A. Eichel, L.G.J. Bert de Haart, Electrochemical and degradation behaviour of single cells comprising Ni-GDC fuel electrode under high temperature steam- and co-electrolysis conditions, J. Power Sources 556 (2023), 232436, https://doi.org/10.1016/j.jpowsour.2022.232436.

[38] C.F. Manken, D. Schafer, R.-A. Eichel, F. Kunz, Automatic data curation and analysis pipeline for electrochemical impedance spectroscopy measurements conducted on solid oxide cell stacks, ECS Trans. 111 (2023) 373–383, https://doi.org/10.1149/11106.0373ecst.

[39] M. Marasi, A.P. Panunzi, L. Duranti, N. Lisi, E. Di Bartolomeo, Enhancing oxygen reduction activity and structural stability of La0.6Sr0.4FeO3-δby 1 mol % Pt and

Ru B-site doping for application in all-perovskite IT-SOFCs, ACS Appl. Energy Mater. 5 (2022) 2918–2928, https://doi.org/10.1021/acsaem.1c03613.
[40] P.K. Dubey, J. Hong, M.R. Anisur, K. Lee, S. Belko, P. Singh, Enhanced electrocatalytic activity and surface exsolution in PrOx-substituted cerium gadolinium oxide, ACS Appl. Energy Mater. 6 (2023) 657–666, https://doi.org/10.1021/acsaem.2c02656.
[41] C. Graves, S.D. Ebbesen, M. Mogensen, Co-electrolysis of CO2 and H2O in solid oxide cells: performance and durability, Solid State Ionics 192 (2011) 398–403, https://doi.org/10.1016/j.ssi.2010.06.014.
[42] F. Ciucci, C. Chen, Analysis of electrochemical impedance spectroscopy data using the distribution of relaxation times: a Bayesian and hierarchical Bayesian approach, Electrochim. Acta 167 (2015) 439–454, https://doi.org/10.1016/j.electacta.2015.03.123.
[43] T.H. Wan, M. Saccoccio, C. Chen, F. Ciucci, Influence of the discretization methods on the distribution of relaxation times deconvolution: implementing radial basis functions with DRTtools, Electrochim. Acta 184 (2015) 483–499, https://doi.org/10.1016/j.electacta.2015.09.097.
[44] B.A. Boukamp, Fourier transform distribution function of relaxation times; application and limitations, Electrochim. Acta 154 (2015) 35–46, https://doi.org/10.1016/j.electacta.2014.12.059.
[45] H. Sumi, T. Yamaguchi, K. Hamamoto, T. Suzuki, Y. Fujishiro, Electrochemical analysis for anode-supported microtubular solid oxide fuel cells in partial reducing and oxidizing conditions, Solid State Ionics 262 (2014) 407–410, https://doi.org/10.1016/j.ssi.2014.01.012.
[46] V. Subotić, C. Schluckner, J. Strasser, V. Lawlor, J. Mathe, J. Rechberger, H. Schroettner, C. Hochenauer, In-situ electrochemical characterization methods for industrial-sized planar solid oxide fuel cells Part I: Methodology, qualification and detection of carbon deposition, Electrochim. Acta 207 (2016) 224–236, https://doi.org/10.1016/j.electacta.2016.05.025.
[47] M. Schonleber, E. Ivers-Tiffée, Approximability of impedance spectra by RC elements and implications for impedance analysis, Electrochem. Commun. 58 (2015) 15–19, https://doi.org/10.1016/j.elecom.2015.05.018.
[48] B.A. Boukamp, A linear kronig-kramers transform test for immittance data validation, J. Electrochem. Soc. 142 (1995) 1885–1894, https://doi.org/10.1149/1.2044210.
[49] T. Bergmann, N. Schlüter, Improved DRT determination through a modified sparse spike deconvolution, ECS Trans. 111 (2023) 413–418, https://doi.org/10.1149/11106.0413ecst.
[50] T.G. Bergmann, N. Schlüter, Introducing alternative algorithms for the determination of the distribution of relaxation times, ChemPhysChem 23 (2022), https://doi.org/10.1002/cphc.202200012.
[51] J. Weese, A reliable and fast method for the solution of Fredholm integral equations of the first kind based on Tikhonov regularization, Comput. Phys. Commun. 69 (1992) 99–111, https://doi.org/10.1016/0010-4655(92)90132-I.
[52] M. Riegraf, R. Costa, G. Schiller, K.A. Friedrich, S. Dierickx, A. Weber, Electrochemical impedance analysis of symmetrical Ni/Gadolinium-Doped ceria (CGO10) electrodes in electrolyte-supported solid oxide cells, J. Electrochem. Soc. 166 (2019) F865–F872, https://doi.org/10.1149/2.0051913jes.
[53] C. Grosselindemann, N. Russner, S. Dierickx, F. Wankmüller, A. Weber, Deconvolution of gas diffusion polarization in Ni/Gadolinium-Doped ceria fuel electrodes, J. Electrochem. Soc. 168 (2021), 124506, https://doi.org/10.1149/1945-7111/ac3d02.
[54] S. Primdahl, Y.L. Liu, Ni catalyst for hydrogen conversion in gadolinia-doped ceria anodes for solid oxide fuel cells, J. Electrochem. Soc. 149 (2002) A1466, https://doi.org/10.1149/1.1514234.
[55] M. Riegraf, V. Yurkiv, R. Costa, G. Schiller, K.A. Friedrich, Evaluation of the effect of sulfur on the performance of nickel/gadolinium-doped ceria based solid oxide fuel cell anodes, ChemSusChem 10 (2017) 587–599, https://doi.org/10.1002/cssc.201601320.
[56] V.A. Rojek-Wockner, A.K. Opitz, M. Brandner, J. Mathé, M. Bram, A novel Ni/ceria-based anode for metal-supported solid oxide fuel cells, J. Power Sources 328 (2016) 65–74, https://doi.org/10.1016/j.jpowsour.2016.07.075.
[57] M. Riegraf, M.P. Hoerlein, R. Costa, G. Schiller, K.A. Friedrich, Sulfur poisoning of electrochemical reformate conversion on nickel/gadolinium-doped ceria electrodes, ACS Catal. 7 (2017) 7760–7771, https://doi.org/10.1021/acscatal.7b02177.
[58] M. Riegraf, R. Costa, G. Schiller, K.A. Friedrich, Sulfur poisoning of Ni/cgo anodes: a long-term degradation study, ECS Trans. 78 (2017) 1285–1291, https://doi.org/10.1149/07801.1285ecst.
[59] A. Kromp, S. Dierickx, A. Leonide, A. Weber, E. Ivers-Tiffée, Electrochemical analysis of sulfur-poisoning in anode supported SOFCs fuelled with a model reformate, J. Electrochem. Soc. 159 (2012) B597–B601, https://doi.org/10.1149/2.015206jes.
[60] J.B. Hansen, Correlating sulfur poisoning of SOFC nickel anodes by a temkin isotherm, Electrochem. Solid State Lett. 11 (2008), https://doi.org/10.1149/1.2960521.
[61] D.R. Huntley, The decomposition of H2S on Ni(110), Surf. Sci. 240 (1990) 13–23, https://doi.org/10.1016/0039-6028(90)90726-O.
[62] C.H. Bartholomew, Mechanisms of catalyst deactivation, Appl. Catal. Gen. 212 (2001) 17–60, https://doi.org/10.1016/S0926-860X(00)00843-7.
[63] S.P.S. Badwal, Effect of dopant concentration on the grain boundary and volume resistivity of yttria-zirconia, J. Mater. Sci. Lett. 6 (1987) 1419–1421, https://doi.org/10.1007/BF01689307.
[64] J.E. Bauerle, Study of solid electrolyte polarization by a complex admittance method, J. Phys. Chem. Solid. 30 (1969) 2657, https://doi.org/10.1016/0022-3697(69)90039-0.
[65] F. Kullmann, C. Grosselindemann, L. Salamon, F. Fuchs, A. Weber, B1507 Investigation of Interface and Electrolyte Processes of a State-Of-The-Art SOFC, 15th European SOFC & SOE Forum, 2022, p. B1507.
[66] S. Golani, F. Wankmüller, W. Herzhof, C. Dellen, N.H. Menzler, A. Weber, Impact of GDC Interlayer Microstructure on Strontium Zirconate Interphase Formation and Cell Performance, 15th European SOFC & SOE Forum, 2022, p. A0901.
[67] A. Tsoga, A. Naoumidis, A. Gupta, D. Stover, Microstructure and interdiffusion phenomena in YSZ-CGO composite electrolyte, Mater. Sci. Forum 308–311 (1999) 794–799. https://doi.org/10.4028/www.scientific.net/msf.308-311.794.
[68] A. Tsoga, A. Naoumidis, D. Stover, Total electrical conductivity and defect structure of ZrO2-CeO2-Y2O3-Gd2O3 solid solutions, Solid State Ionics 135 (2000) 403–409, https://doi.org/10.1016/S0167-2738(00)00477-X.
[69] S. Wang, T. Kobayashi, M. Dokiya, T. Hashimoto, Electrical and ionic conductivity of Gd-doped ceria, J. Electrochem. Soc. 147 (2000) 3606–3609, https://doi.org/10.1149/1.1393946.
[70] V.P. Gorelov, V.B. Balakireva, I.Y. Yaroslavtsev, V.A. Kazantsev, E.G. Vaganov, Conductivity and thermal expansion of the Ce0.8Gd 0.2O1.9 solid electrolyte in the oxidizing and reducing atmospheres, Russ. J. Electrochem. 43 (2007) 888–893, https://doi.org/10.1134/S102319350708006X.
[71] A. Utz, A. Leonide, A. Weber, E. Ivers-Tiffée, Studying the CO-CO2 characteristics of SOFC anodes by means of patterned Ni anodes, J. Power Sources 196 (2011) 7217–7224, https://doi.org/10.1016/j.jpowsour.2010.10.056.
[72] A. Utz, H. Stormer, A. Leonide, A. Weber, E. Ivers-Tiffée, Degradation and relaxation effects of Ni patterned anodes in H2–H2O atmosphere, J. Electrochem. Soc. 157 (2010) B920, https://doi.org/10.1149/1.3383041.
[73] S.R. Bishop, K.L. Duncan, E.D. Wachsman, Surface and bulk oxygen non-stoichiometry and bulk chemical expansion in gadolinium-doped cerium oxide, Acta Mater. 57 (2009) 3596–3605, https://doi.org/10.1016/j.actamat.2009.04.017.
[74] B. Mirfakhraei, S. Paulson, V. Thangadurai, V. Birss, Enhanced hydrogen oxidation activity and H2S tolerance of Ni-infiltrated ceria solid oxide fuel cell anodes, J. Power Sources 243 (2013) 95–101, https://doi.org/10.1016/j.jpowsour.2013.05.150.